Effect of Warm Rolling on the Structure and Tensile Properties of a Metastable Fe-Based Medium Entropy Alloy

Hyojin Park[1,2] · Jungwan Lee[1,2] · Rae Eon Kim[2,3] · Sujung Son[1,2] · Soung Yeoul Ahn[1,2] · Hyoung Seop Kim[2,3,4,5]

Abstract

The present study investigates the impact of warm rolling on the microstructure and tensile properties of $Fe_{60}(CoNi)_{30}Cr_{10}$ Fe-based medium entropy alloy (Fe-MEA). Warm rolling is performed above room temperature but below the recrystallization temperature. The experimental procedures involve comparing the microstructure and mechanical properties of the warm-rolled specimen with a cold-rolled and subsequently annealed specimen. Microstructural analysis reveals coarse elongated face-centered cubic grains, deformation-induced martensite, and a high density of dislocations in the warm-rolled sample. Tensile tests conducted at ambient and cryogenic temperatures demonstrate that the warm-rolled Fe-MEA exhibits enhanced strength and a similar level of elongation compared to the annealed sample. The improved mechanical properties are attributed to the transformation-induced plasticity resulting from the high dislocation density by warm rolling. This study provides valuable insights into the potential of warm rolling as a processing technique to enhance the mechanical properties of Fe-MEA, offering possibilities for broader applications.

Keywords Ferrous medium entropy alloy · Warm rolling · Thermal–mechanical processing · Transformation induced plasticity

1 Introduction

Extensive research has been studied on numerous high entropy alloys (HEAs) and medium entropy alloys (MEAs), which offer a wide range of elemental combinations [1–5]. These HEAs/MEAs have demonstrated remarkable mechanical properties, including tensile strength [2, 6], fatigue resistance [7], creep resistance [8], anti-fouling properties [9], and superplasticity [10–12]. Among the various HEAs/MEAs, Fe-based medium entropy alloys (Fe-MEAs) with a high Fe concentration have emerged as promising candidates for commercialization due to their cost-effectiveness and superior mechanical performance [13, 14]. By design, Fe-MEAs exhibit a metastable face-centered cubic (FCC) phase, enabling transformation-induced plasticity (TRIP) as predicted by thermodynamic calculations [13–15]. This design approach has led to Fe-MEAs with an attractive combination of strength and ductility, displaying exceptional TRIP behavior [13–16]. Moreover, the properties of Fe-MEAs can be significantly enhanced through adjustments in thermal–mechanical processing (TMP) [17–20]. However, it is worth noting that the superior properties of Fe-MEAs are primarily achieved at cryogenic temperatures, and their yield strength (YS) is comparatively lower at ambient temperature (298 K) than those of conventional alloys, a common characteristic of single FCC alloys [13, 21–23].

To expand the potential applications of Fe-MEAs, it is essential to gain a comprehensive understanding of their TMP behavior. By tailoring microstructure through

✉ Hyoung Seop Kim
hskim@postech.ac.kr

1 Department of Materials Science and Engineering, Pohang University of Science and Technology (POSTECH), Pohang 37673, Republic of Korea

2 Center for Heterogenic Metal Additive Manufacturing, Pohang University of Science and Technology (POSTECH), Pohang 37673, Republic of Korea

3 Graduate Institute of Ferrous Technology, Pohang University of Science and Technology (POSTECH), Pohang 37673, Republic of Korea

4 Institute for Convergence Research and Education in Advanced Technology, Yonsei University, Seoul 03722, Republic of Korea

5 Advanced Institute for Materials Research (WPI-AIMR), Tohoku University, Sendai 980-8577, Japan

appropriate TMP, it becomes possible to achieve superior mechanical properties [17–20, 24–29]. Previous studies have focused on the structural and mechanical properties of as-rolled HEAs/MEAs [25–28, 30, 31], with cold and cryo-rolled alloys displaying unexpected microstructure and enhanced YS [25–28, 30, 32]. However, the investigation of warm rolling, a technique performed above room temperature but below the recrystallization temperature, has been limited in the field of HEAs/MEAs. Warm rolling offers distinct advantages over cold and cryogenic rolling method, such as reduced applied flow stress [31] and promotion of dynamic recovery in highly dense dislocations due to the warm temperature [33]. As a result, warm rolling enable to improve the YS and to reach a similar level of ductility compared to well-recrystallized annealed sample. Furthermore, warm rolling can significantly reduce processing steps, costs, and time associated with TMP. Therefore, this study aims to examine the effect of warm rolling on the microstructure and mechanical properties of the metastable FCC phase $Fe_{60}(CoNi)_{30}Cr_{10}$ MEA.

2 Experimental Procedures

The $Fe_{60}Co_{15}Ni_{15}Cr_{10}$ (at%) Fe-MEA of 150 g was cast using vacuum induction melting (MC100V, Indutherm) with high-purity elements (> 99% purity) in graphite mold (50 mm × 35 mm × 7 mm). The 150 g ingot was homogenized at 1373 K for 6 h, followed by water quenching. Subsequently, the ingot was warm rolled at 773 K with a thickness reduction ratio of 10% per rolling pass and a total reduction of 62%. After every two rolling passes, the ingot was reheated for 10 min at 773 K to maintain the temperature. The warm-rolled Fe-MEA is denoted as "WR". For comparison, another as-homogenized ingot was cold-rolled at ambient temperature with a thickness reduction ratio of 79%. The cold-rolled plate was annealed at 1073 K for 10 min to achieve full recrystallized grain, followed by immediate water quenching. The sample is named as "CR + AN". The TMP are schematically illustrated in Fig. 1. Dog-bone-shaped tensile specimens were obtained by electrical discharge machining, with gauge length, width, and thickness of $1.5 \times 1 \times 1.5$ mm^3. The 1.5 mm gauge length samples were subjected to tensile deformation at 298 K and at 77 K using universal testing equipment (Instron Corp., Instron 1361) at a constant strain rate of 10^{-3} s^{-1}. During the tensile tests at 298 K, the local plastic strain was measured using a digital image correlation (DIC) method (ARAMIS 12M, GOM Optical Measuring Techniques). For the tensile tests at 77 K, the gauge length of the samples was marked using a microhardness tester in order to accurately calculate the tensile elongation, and a liquid nitrogen chamber was attached to the tensile testing equipment to maintain
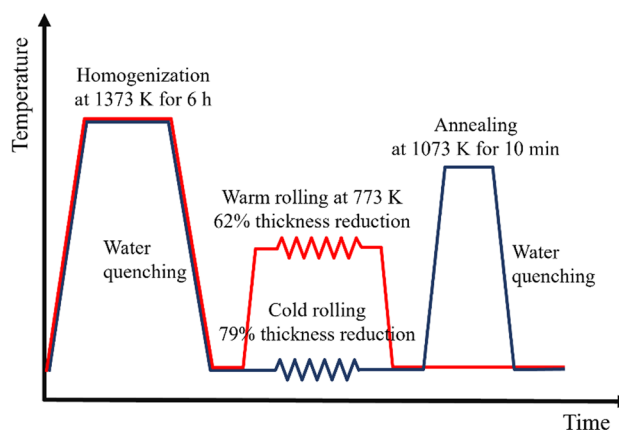

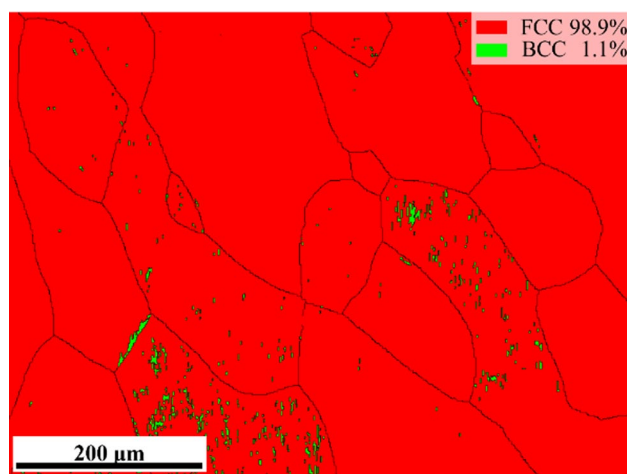**Fig. 1** Schematic of warm rolling and cold rolling followed by annealing

Fig. 2 EBSD phase map of the homogenized specimen

a temperature of 77 K. The microstructures of the homogenized, WR, CR + AN, and deformed tensile samples were analyzed using scanning electron microscopy-electron backscatter diffraction (SEM-EBSD) (JEOL, JSM-7100), field emission-scanning electron microscopy (FE-SEM) with back-scattered electron (BSE), and energy dispersive X-ray spectroscopy (EDS).

3 Results and Discussion

The homogenized specimen displays coarse FCC grains whose average size exceeds 150 µm, as shown in Fig. 2. Figure S1 presents the BSE images and EDS maps of the WR and CR + AN specimens, respectively. The WR specimen is highly deformed, and the grain boundaries are not clearly defined, whereas the CR + AN specimen exhibits distinct grain boundary and the equiaxed grains.

Additionally, both WR and CR + AN specimens demonstrate the absence of element segregation, which is consistent with the result of the previous study [13]. In HEAs/MEAs, the high mixing entropy enhances the mutual solubility between elements and the stability of solution phases rather than inducing elemental segregation [34, 35].

Microstructure analysis reveals clear distinctions between the CR + AN and WR specimens. The CR + AN specimen exhibits a nearly-fully FCC phase with an average grain size of 9.41 ± 2.39 μm (excluding twin boundaries), as shown in Fig. 3a. A small amount of thermally induced martensite is observed due to water quenching. Phase and inverse pole figure (IPF) maps in Fig. 3a and b also illustrate the presence of abundant annealing twin in the CR + AN specimen. The kernel average misorientation (KAM) map provides insights into the geometrically necessary dislocation (GND) density and plastic strain distribution within the specimens [36, 37, 38]. The KAM map of the CR + AN specimen (Fig. 3c) shows values below 0.5°, indicating a recrystallized microstructure characterized by a relatively low GND density. In contrast, the WR specimen exhibits coarse elongated grains in FCC phase, aligned along the rolling direction (RD), accompanied by body-centered cubic (BCC) grains inclined at approximately 35° to the RD (Fig. 3d). Figure 3e depicts the internal deformation of a grain in the IPF map of the WR sample. This distinctive microstructure is a result of the warm rolling process. Warm rolling applies substantial force to the material while allowing dynamic recovery due to its elevated temperature. As a result, the material undergoes a moderate strain, which is comparatively less than that experienced cold rolling and cryo-rolling. Therefore, in the WR specimen, dynamically recovered highly-dense dislocations and a small amount of deformation-induced martensite are present in the matrix while maintaining a large grain size. Furthermore, the small amount of martensite and nucleation site for martensite are generated by the moderate strain and coarse grain size of the homogenized specimen (as presented in Fig. 2). It is believed that the lower stress is required to initiate TRIP in coarse grain [36, 37], thereby contributing to the formation of martensite and nucleation sites [39].

Additionally, the KAM map of the WR specimen (Fig. 3f) reveals higher KAM values exceeding 3.5°, indicating an elevated GND density resulting from the accumulation of substantial strain during the warm rolling process.

The engineering stress–strain curves of the WR and CR + AN specimens at ambient temperature and cryogenic temperature are presented in Fig. 4a and 4b, respectively. Table 1 provides a comprehensive summary of the tensile properties of both specimens at these temperatures. At ambient temperature, the CR + AN specimen exhibits a high total elongation (~ 70%) but low strengths, with a YS of 248 MPa and ultimate tensile strength (UTS) of 552 MPa. In contrast, the WR specimen demonstrates a superior combination of strength and ductility, with YS, UTS, and total elongation of 575 MPa, 679 MPa, and 55%, respectively. At cryogenic temperature, the WR specimen shows higher YS of 701 MPa, UTS of 1541 MPa, and slightly reduced total elongation (43%) compared to the CR + AN; YS, UTS, and
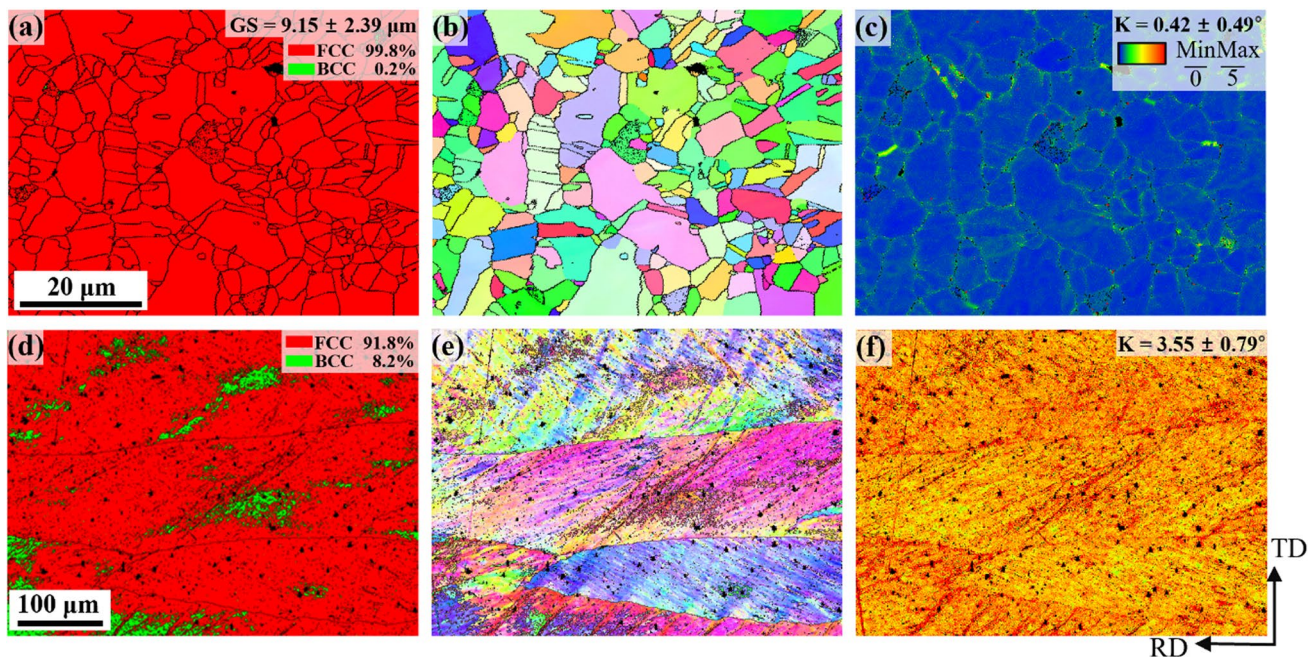
Fig. 3 EBSD images of the CR + AN specimen: **a** phase map, **b** IPF map, and **c** KAM map. EBSD images of the WR sample: **d** phase map, **e** IPF, and **f** KAM map

Fig. 4 Engineering stress–strain curves of the WR and CR + AN specimens at **a** 298 K and **b** 77 K. SHR and true stress–strain curves (true) of WR at **c** 298 K and **d** 77 K
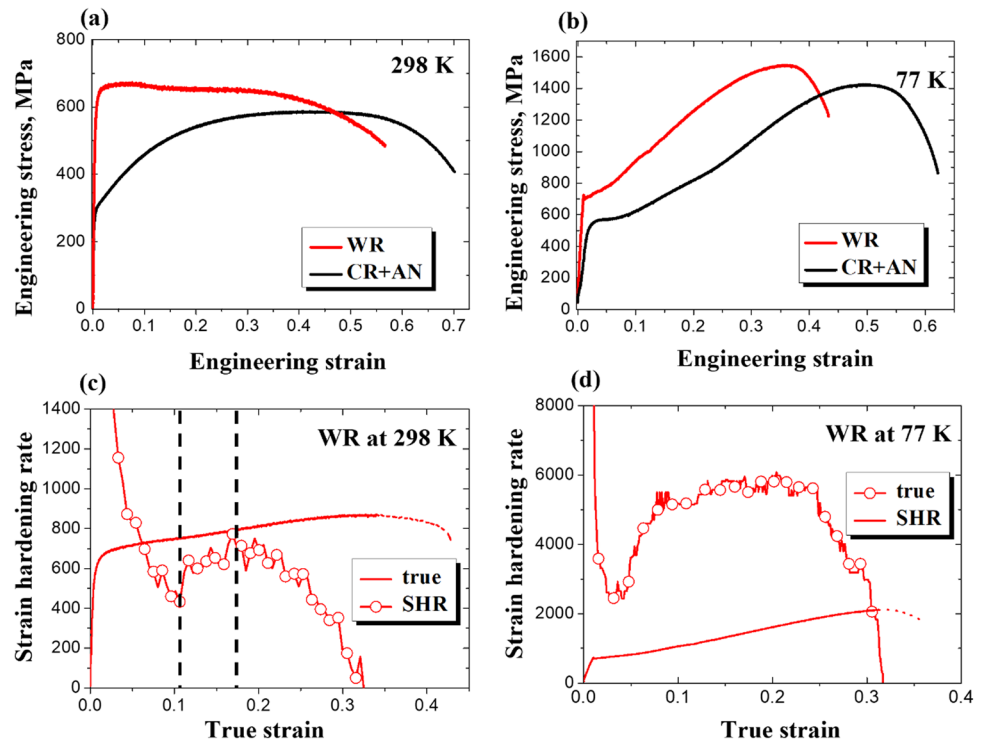
**Table 1** Ambient temperature and cryogenic temperature tensile properties of CR + AN and WR samples

Temperature, K	Specimen	YS, MPa	UTS, MPa	TE, %
298 K	CR + AN	248.2 ± 27.8	552.4 ± 34.3	69.98 ± 0.0
	WR	575.1 ± 4.0	679.5 ± 6.7	54.9 ± 0.7
77 K	CR + AN	532.0 ± 53. 1	1436.5 ± 14.2	54.20 ± 0.2
	WR	701.0 ± 3.1	1540.9 ± 6.1	43.0 ± 0.3

total elongation of 532 MPa, 1436 MPa, and 54%, respectively. The significant enhancement in YS can be attributed to the presence of a high density of dislocations and deformation-induced martensite, which exhibits high Peierls lattice friction stress [40], which compensate the grain boundary strengthening. At ambient temperature, the remarkable elongation of the WR specimen, reaching up to 55%. The onset of necking is identified as the point of intersection between the true stress–strain curve and the strain hardening rate (SHR) curve [41, 42]. Notably, the true stress–strain curve of the WR specimen exhibits two distinct intersections with its corresponding SHR curve (Fig. 4c), a phenomenon previously observed in the same alloy fabricated using selective laser melting [43]. On the other hand, WR specimen has a typical single necking point at cryogenic temperature deformation.

The utilization of DIC analysis provides valuable insights into the distribution of localized plastic strain within the

tensile-deformed WR specimen. Figure 5 visually depicts the DIC images overlaid with the corresponding local true strain distribution at different engineering strain levels. At an engineering strain (ε_{eng}) of 6.8%, localized plastic strain is observed primarily at the upper part of the gauge, indicating the initiation of the first necking (Fig. 5a). Interestingly, as the global engineering strain increases, the localized strain at the upper gauge is gradually relieved and repositioned to the center of the gauge, as depicted in Fig. 5b and c (The video version of the DIC strain map is shown in Supplementary Video 1). The alleviation of strain localization suggests the emergence of an additional strengthening mechanism, which will be discussed in detail in the subsequent paragraph. Notably, at an ε_{eng} of 23.3% in Fig. 5d, intense localized strain at the middle part of the gauge indicates the occurrence of the second necking. The presence of these two distinct necking events at ε_{eng} 6.8% and 23.3% highlights the unique mechanical behavior exhibited by the WR specimen. The delayed progression of the first necking can be attributed to an additional strengthening mechanism, consequently contributing to an increase in elongation.

To further investigate the additional strengthening mechanism at ambient temperature in the WR specimen, EBSD analysis is performed on the deformed microstructures at various local strains. At local ε_{eng} 6.8%, no significant phase transformation is observed, indicating that the dominant mechanism during tensile deformation is Taylor strengthening due to the high level of plastic strain (Fig. 6a). Taylor strengthening is a phenomenon in which the presence of
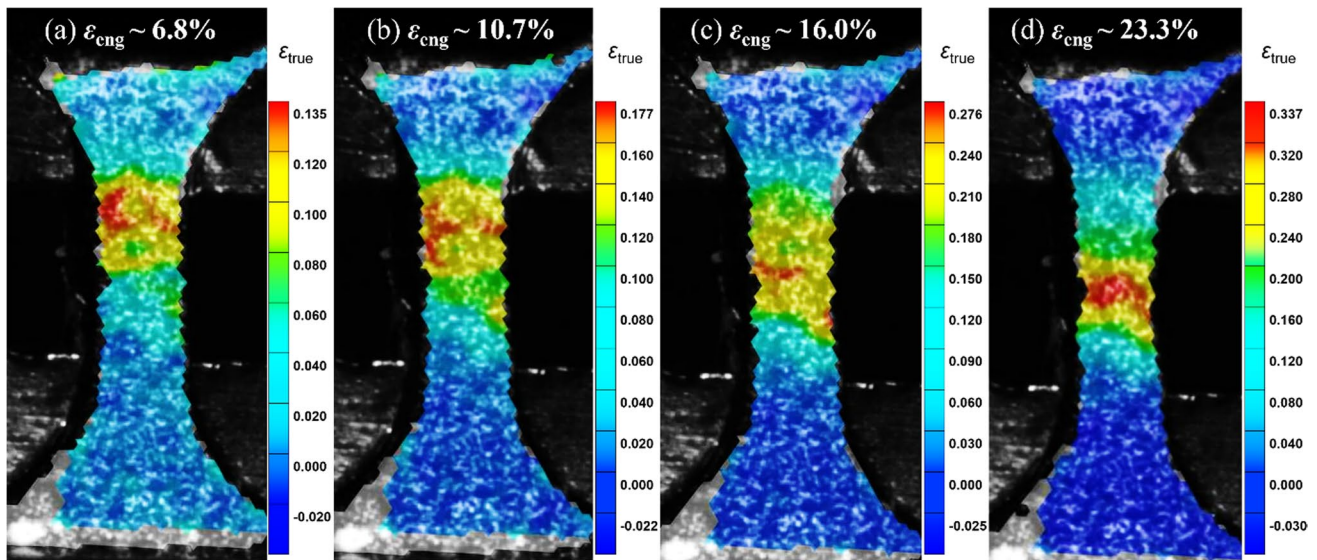
Fig. 5 a–d Local true strain distribution with an increase in engineering strain (ε_{eng}) on the tensile-deformed WR specimen at 298 K, obtained using the DIC technique. The scale bars are created based on the highest and lowest local true strain value of each ε_{eng}
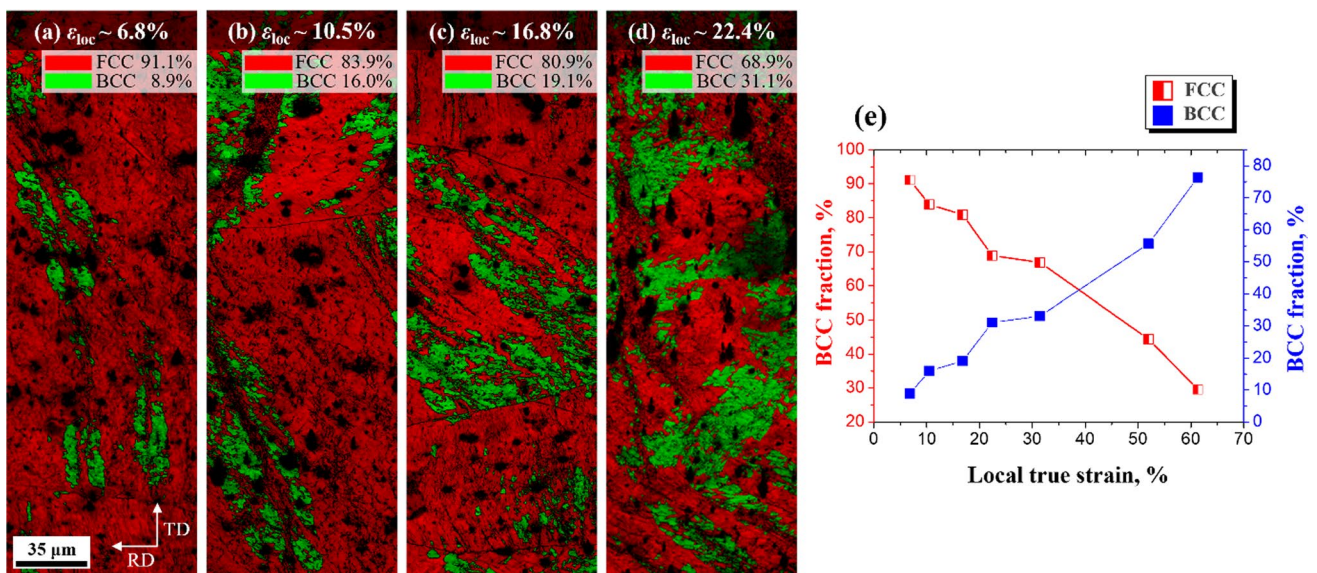
Fig. 6 EBSD phase maps of deformed microstructure of WR **a–d** at different local engineering strain (ε_{loc}) levels and **e** phase fraction plot of WR specimen

dislocations within a material hinders the mobility of other dislocations, resulting in an enhancement in the strength of material [44]. The WR specimen exhibits a higher GND density compared to the CR + AN specimen due to warm rolling's inherent dynamic recovery without any additional heat treatment (as depicted in Fig. 3). Notably, this strengthening mechanism is particularly prominent in materials with a higher dislocation concentration. The highly dense dislocation creates a lattice structure with more obstacles, thus making it harder for dislocations to glide or move within

the crystal lattice [45]. In the WR specimen, the presence of the higher dislocation obstructs the movement of dislocations, making it difficult for dislocation to glide each other. The interaction of dislocations leads to an increase in strain hardening and also contributes to an enhanced yield strength [46]. Whereas, at the local ε_{eng} 10.5% (Fig. 6b), the fraction of the BCC phase fraction starts to increase from the initial value of 6.8%. As the local ε_{eng} 16.8% (Fig. 6c), the BCC phase fraction reaches 19.1%. The occurrence of deformation-induced martensitic transformation is confirmed by a

positive slope in the SHR curve (Fig. 4c). The WR specimen demonstrates the ability to deform without severe strain localization due to the enhanced capacity of dislocation accommodation aided by TRIP (Fig. 6c). This suggests that TRIP serves as an additional deformation mechanism, contributing to the delay in necking progression. Subsequently, after the second necking, the localized tensile strain in the necking region promotes the occurrence of deformation-induced martensitic transformation, further contributing to the overall elongation of the WR specimen. At local ε_{eng} 22.4% (Fig. 6d), the BCC fraction reaches 31.1%. Observation near the fracture surface reveals that the BCC phase fraction reaches up to 80% (see Fig. 6e), which is significantly higher than that of the CR + AN specimen, where only 19.7% of the BCC was observed (Fig. S2). The WR specimen experiences significant TRIP for the following reasons. The coarse FCC grains in the WR specimen lead to lower FCC stability than fine-grained material, thereby facilitating the propagation of TRIP within the grains [36, 47]. During the warm rolling, a high density of GND is generated, allowing the alloy to overcome an energy barrier for the FCC to BCC phase transformation [48, 49]. The high GND density controls the occurrence of TRIP. Therefore, the combined effect of TRIP and Taylor strengthening contributes to the delay of necking progression and the improvement of elongation of WR specimen. Consequently, the WR specimen exhibits a better combination of strength and ductility compared to the CR + AN specimen during deformation at ambient temperature. Based on these results, warm rolling can be expected to offer improved mechanical properties in FCC materials where dislocation activity serves as a primary deformation mechanism, and active TRIP behavior is absent. By employing warm rolling instead of annealing subsequent to cold rolling, it becomes possible to surmount the low YS and enhance work hardening. These are achieved by augmenting the dislocation density within the matrix while simultaneously preserving exceptional ductility through the introduction of active TRIP.

The microstructures of the deformed WR specimen at cryogenic temperatures are further analyzed with respect to local true strain (ε_{tr}). In Fig. S3, the fraction of the BCC phase reaches 76.7% at ε_{tr} of only 7.0%, and it further increases to 88.3% at ε_{tr} of 11.5%. These results indicate the occurrence of accelerated TRIP at the early stage of deformation. It is well known that the stability of the FCC phase in the alloy decreases with decreasing temperature, as evidenced by the Gibbs free energy of the FCC to BCC phase transformation [13, 50, 51]. The decreased stability of FCC phase at cryogenic temperatures facilitates the rapid initiation of TRIP in the WR specimen. Additionally, warm rolling demonstrates the ability to enhance the YS of the alloy without significantly sacrificing elongation, both at ambient and cryogenic temperatures.

4 Conclusion

In conclusion, this study investigated the mechanical properties of the $Fe_{60}(CoNi)_{30}Cr_{10}$ Fe-MEA alloy subjected to warm rolling at ambient temperature and cryogenic temperature. The results demonstrate that warm rolling provides advantages to the Fe-MEA, resulting in improved combination of strength and ductility during ambient temperature tensile testing. The warm rolling process induces dynamic recovery, allowing for the accommodation of highly dense GND and promoting TRIP during the tensile deformation. Additionally, warm rolling offers streamlined and simplified thermal–mechanical process step compared to the conventional cold rolling followed by annealing process. This research highlights the effectiveness of warm rolling as a strategic method for tuning the microstructure and phase stability of Fe-MEA, introducing a novel approach that improves processing efficiency in the field.

Declaration

Competing Interests The authors declare that one of the authors (H. S. Kim) is the editor of Metals and Materials International.

References

1. B. Cantor, I.T.H. Chang, P. Knight, A.J.B. Vincent, Microstructure development in equiatomic multicomponent alloys. Mater. Sci. Eng. A **375-377**, 213–218 (2004). https://doi.org/10.1016/j.msea.2003.10.257

2. Z. Li, K.G. Pradeep, Y. Deng, C.C. Tasan, Metastable high-entropy dual-phase alloys overcome the strength–ductility trade-off. Nature **534**, 227–230 (2016). https://doi.org/10.1038/nature17981

3. Y.A. Alshataif, S. Sivasankaran, F.A. Al-Mufadi, A.S. Alaboodi, H.R. Ammar, Manufacturing methods, microstructural and mechanical properties evolutions of high-entropy alloys: a review. Met. Mater. Int. **26**, 1099–1133 (2020). https://doi.org/10.1007/s12540-019-00565-z

4. B. Gludovatz, A. Hohenwarter, K.V.S. Thurston, H. Bei, Z. Wu, E.P. George, Exceptional damage-tolerance of a medium-entropy alloy CrCoNi at cryogenic temperatures. Nat. Commun. **7**, 10602 (2016). https://doi.org/10.1038/ncomms10602

5. L. Xia, Q. Wu, K. Zhou, F. He, Z. Wang, Concurrent recrystallization and precipitation for combination of superior precipitation and grain boundary hardening in Co37Cr20Ni37Ti3Al3

high-entropy alloy. Met. Mater. Int. **28**, 2863–2873 (2022). https://doi.org/10.1007/s12540-022-01178-9

6. H. Zhou, Y. Lin, F. Chen, O. Shen, Effect of precipitation behavior on mechanical properties of a Nb-containing CoCrNi-based high-entropy alloy. Met. Mater. Int. **29**, 674–692 (2023). https://doi.org/10.1007/s12540-022-01265-x

7. G.T. Lee, J.W. Won, K.R. Lim, M. Kang, H.J. Kwon, Y.S. Na, Y.J. Choi, Effect of microstructural features on the high-cycle fatigue behavior of CoCrFeMnNi high-entropy alloys deformed at room and cryogenic temperatures. Met. Mater. Int. **27**, 593–602 (2021). https://doi.org/10.1007/s12540-020-00786-7

8. Y.B. Kang, S.H. Shim, K.H. Lee, S.I. Hong, Dislocation creep behavior of CoCrFeMnNi high entropy alloy at intermediate temperatures. Mater. Res. Lett. **6**, 689–695 (2018). https://doi.org/10.1080/21663831.2018.1543731

9. S. Son, S. Kim, J. Kwak, G.H. Gu, D.S. Hwang, Y.-T. Kim, H.S. Kim, Superior antifouling properties of a CoCrFeMnNi high-entropy alloy. Mater. Lett. **300**, 130130 (2021). https://doi.org/10.1016/j.matlet.2021.130130

10. N.T.-C. Nguyen, P. Asghari-Rad, P. Sathiyamoorthi, A. Zargaran, C.S. Lee, H.S. Kim, Ultrahigh high-strain-rate superplasticity in a nanostructured high-entropy alloy. Nat. Commun. **11**, 2736 (2020). https://doi.org/10.1038/s41467-020-16601-1

11. S.S. Nene, K. Liu, S. Sinha, M. Frank, S. Williams, R.S. Mishra, Superplasticity in fine grained dual phase high entropy alloy. Mater. **9**, 100521 (2020). https://doi.org/10.1016/j.mtla.2019.100521

12. H. Park, N.T.-C. Nguyen, P. Sathiyamoorthi, S. Son, J. Moon, H.S. Kim, Superplastic behavior of Al15(CuFeMn)85 immiscible medium-entropy alloy. Intermetallics **157**, 107883 (2023). https://doi.org/10.1016/j.intermet.2023.107883

13. J.W. Bae, J.B. Seol, J. Moon, S.S. Sohn, M.J. Jang, H.Y. Um, B.-J. Lee, H.S. Kim, Exceptional phase-transformation strengthening of ferrous medium-entropy alloys at cryogenic temperatures. Acta Mater. **161**, 388–399 (2018). https://doi.org/10.1016/j.actamat.2018.09.057

14. J.W. Bae, H.S. Kim, Towards ferrous medium-entropy alloys with low-cost and high-performance. Scr. Mater. **186**, 169–173 (2020). https://doi.org/10.1016/j.scriptamat.2020.05.030

15. D.G. Kim, Y.H. Jo, J. Yang, W.-M. Choi, H.S. Kim, B.-J. Lee, S.S. Sohn, S. Lee, Ultrastrong duplex high-entropy alloy with 2 GPa cryogenic strength enabled by an accelerated martensitic transformation. Scr. Mater. **171**, 67–72 (2019). https://doi.org/10.1016/j.scriptamat.2019.06.026

16. H.D. Park, J.W. Won, J. Moon, H.S. Kim, H. Sung, J.B. Seol, J.W. Bae, J.G. Kim, Fe55Co17.5Ni10Cr12.5Mo5 high-entropy alloy with outstanding cryogenic mechanical properties driven by deformation-induced phase transformation behavior. Met. Mater. Int. **29**, 95–107 (2023). https://doi.org/10.1007/s12540-022-01215-7

17. H. Kwon, S. Harjo, T. Kawasaki, W. Gong, S.G. Jeong, E.S. Kim, P. Sathiyamoorthi, H. Kato, H.S. Kim, Work hardening behavior of hot-rolled metastable Fe50Co25Ni10Al5Ti5Mo5 medium-entropy alloy: in situ neutron diffraction analysis. Sci. Technol. Adv. Mater. **23**, 579–586 (2022). https://doi.org/10.1080/14686996.2022.2122868

18. F. Haftlang, P. Asghari-Rad, J. Moon, S. Lee, H. Kato, H.S. Kim, Superior phase transformation-assisted mechanical properties of a metastable medium-entropy ferrous alloy with heterogeneous microstructure. Mater. Lett. **302**, 130391 (2021). https://doi.org/10.1016/j.matlet.2021.130391

19. J.W. Bae, J. Lee, A. Zargaran, H.S. Kim, Enhanced cryogenic tensile properties with multi-stage strain hardening through partial recrystallization in a ferrous medium-entropy alloy. Scr. Mater. **194**, 113653 (2021). https://doi.org/10.1016/j.scriptamat.2020.113653

20. J. Lee, J.W. Bae, P. Asghari-Rad, H.S. Kim, Double-humped strain hardening in a metastable ferrous medium-entropy alloy by cryogenic pre-straining and subsequent heat treatment. Scr. Mater. **211**, 114511 (2022). https://doi.org/10.1016/j.scriptamat.2022.114511

21. D.G. Kim, Y.H. Jo, J.M. Park, W.-M. Choi, H.S. Kim, B.-J. Lee, S.S. Sohn, S. Lee, Effects of annealing temperature on microstructures and tensile properties of a single FCC phase CoCuMnNi high-entropy alloy. J. Alloys Compd. **812**, 152111 (2020). https://doi.org/10.1016/j.jallcom.2019.152111

22. J. Yang, Y.H. Jo, D.W. Kim, W.-M. Choi, H.S. Kim, B.-J. Lee, S.S. Sohn, S. Lee, Effects of transformation-induced plasticity (TRIP) on tensile property improvement of Fe45Co30Cr10V10Ni5-xMnx high-entropy alloys. Mater. Sci. Eng. A **772**, 138809 (2020). https://doi.org/10.1016/j.msea.2019.138809

23. M. Harivandi, M. Malekan, S.A. Seyyed Ebrahimi, Soft magnetic high entropy FeCoNiCuMn alloy with excellent ductility and high electrical resistance. Met. Mater. Int. **28**, 556–564 (2022). https://doi.org/10.1007/s12540-021-01111-6

24. Y.A. Alshataif, S. Sivasankaran, F.A. Al-Mufadi, A.S. Alaboodi, H.R. Ammar, Synthesis, microstructures and mechanical behaviour of Cr0.21Fe0.20Al0.41Cu0.18 and Cr0.14Fe0.13Al0.26Cu0.11Si0.25Zn0.11 nanocrystallite entropy alloys prepared by mechanical alloying and hot-pressing. Met. Mater. Int. **27**, 139–155 (2021). https://doi.org/10.1007/s12540-020-00660-6

25. S. Liu, K. Luo, H. Gu, H. Gao, C. Kong, H. Yu, Phase reversion-induced heterogeneous structure in a ferrous medium-entropy alloy via cryorolling and annealing. Scr. Mater. **222**, 115004 (2023). https://doi.org/10.1016/j.scriptamat.2022.115004

26. N. Stepanov, M. Tikhonovsky, N. Yurchenko, D. Zyabkin, M. Klimova, S. Zherebtsov, A. Efimov, G. Salishchev, Effect of cryo-deformation on structure and properties of CoCrFeNiMn high-entropy alloy. Intermetallics **59**, 8–17 (2015). https://doi.org/10.1016/j.intermet.2014.12.004

27. J. Hou, M. Zhang, S. Ma, P.K. Liaw, Y. Zhang, J. Qiao, Strengthening in Al05CoCrFeNi high-entropy alloys by cold rolling. Mater. Sci. Eng. A **707**, 593–601 (2017). https://doi.org/10.1016/j.msea.2017.09.089

28. E. Povolyaeva, S. Mironov, D. Shaysultanov, N. Stepanov, S. Zherebtsov, Outstanding cryogenic strength-ductility properties of a cold-rolled medium-entropy TRIP Fe65(CoNi)25Cr9·5C0.5 alloy. Mater. Sci. Eng. A **836**, 142720 (2022). https://doi.org/10.1016/j.msea.2022.142720

29. J. Yi, L. Yang, L. Wang, L. Liu, Equiatomic, Cu-containing CrCuFeTiV 3d transition metal high entropy alloy with an enhanced strength and hardness synergy. Met. Mater. Int. **28**, 227–236 (2022). https://doi.org/10.1007/s12540-021-00990-z

30. A. Shabani, M.R. Toroghinejad, A. Shafyei, P. Cavaliere, Effect of cold-rolling on microstructure, texture and mechanical properties of an equiatomic FeCrCuMnNi high entropy alloy. Mater. **1**, 175–184 (2018). https://doi.org/10.1016/j.mtla.2018.06.004

31. J. Saha, G. Ummethala, S.R.K. Malladi, P.P. Bhattacharjee, Severe warm-rolling mediated microstructure and texture of equiatomic CoCrFeMnNi high entropy alloy: A comparison with cold-rolling. Intermetallics **129**, 107029 (2021). https://doi.org/10.1016/j.intermet.2020.107029

32. L. Wang, Z. Feng, H. Niu, O. Gao, M. Xu, L. Yang, J. Yi. Study on microstructure and mechanical properties of CrCuFeNiV multi principal element alloy. Met. Mater. Int. **28**, 2987–2996 (2022). https://doi.org/10.1007/s12540-022-01196-7

33. G. Sun, L. Du, J. Hu, B. Zhang, R.D.K. Misra, On the influence of deformation mechanism during cold and warm rolling on annealing behavior of a 304 stainless steel. Mate. Sci. Eng. A **746**, 341–355 (2019). https://doi.org/10.1016/j.msea.2019.01.020

34. K.-Y. Tsai, M.-H. Tsai, J.-W. Yeh, Sluggish diffusion in Co–Cr–Fe–Mn–Ni high-entropy alloys. Acta Mater. **61**, 4887–4897 (2013). https://doi.org/10.1016/j.actamat.2013.04.058

35. J.W. Yeh, S.J. Lin, T.-S. Chin, J.-Y. Gan, S.-K. Chen, T.-T. Shun, C.-H. Tsau, S.-Y. Chou, Formation of simple crystal structures in Cu-Co-Ni-Cr-Al-Fe-Ti-V alloys with multiprincipal metallic elements. Metall. Mater. Trans. A **35**, 2533–2536 (2004). https://doi.org/10.1007/s11661-006-0234-4

36. Z.F. He, N. Jia, D. Ma, H.L. Yan, Z.M. Li, D. Raabe, Joint contribution of transformation and twinning to the high strength-ductility combination of a FeMnCoCr high entropy alloy at cryogenic temperatures. Mater. Sci. Eng. A **759**, 437–447 (2019). https://doi.org/10.1016/j.msea.2019.05.057

37. Z. Li, C.C. Tasan, K.G. Pradeep, D. Raabe, A TRIP-assisted dual-phase high-entropy alloy: Grain size and phase fraction effects on deformation behavior. Acta Mater. **131**, 323–335 (2017). https://doi.org/10.1016/j.actamat.2017.03.069

38. Y. Song, W. Peterson, Theoretical study for dynamic strain aging in niobium: effect of temperature and strain rate on the flow stress. Met. Mater. Int. **28**, 589–602 (2022). https://doi.org/10.1007/s12540-020-00902-7

39. G.B. Olson, M. Cohen, A mechanism for the strain-induced nucleation of martensitic transformations. J. Less-Common Met. **28**, 107–118 (1972). https://doi.org/10.1016/0022-5088(72)90173-7

40. M.R. Gilbert, P. Schuck, B. Sadigh, J. Marian, Free energy generalization of the Peierls potential in iron. Phys. Rev. Lett. **111**, 095502 (2013). https://doi.org/10.1103/PhysRevLett.111.095502

41. T.S. Byun, N. Hashimoto, K. Farrell, Temperature dependence of strain hardening and plastic instability behaviors in austenitic stainless steels. Acta Mater. **52**, 3889–3899 (2004). https://doi.org/10.1016/j.actamat.2004.05.003

42. G.E. Dieter, *Mechanical Metallurgy*, 3rd edn. (McGra-Hill, New York, 1986)

43. J.M. Park, P. Asghari-Rad, A. Zargaran, J.W. Bae, J. Moon, H. Kwon, H.S. Kim, Nano-scale heterogeneity-driven metastability engineering in ferrous medium-entropy alloy induced by additive manufacturing. Acta Mater. **221**, 117426 (2021). https://doi.org/10.1016/j.actamat.2021.117426

44. A.V. Podolskiy, Y.O. Shapovalov, E.D. Tabachnikova, A.S. Tortika, M.A. Tikhonovsky, B. Joni, E. Ódor, T. Ungar, S. Maier, C. Rentenberger, M.J. Zehetbauer, E. Schafler, Anomalous evolution of strength and microstructure of high-entropy Alloy CoCrFeNiMn after high-pressure torsion at 300 and 77 K. Adv. Eng. Mater. **22**, 1900752 (2020). https://doi.org/10.1002/adem.201900752

45. J.G. Kim, N.A. Enikeev, J.B. Seol, M.M. Abramova, M.V. Karavaeva, R.Z. Valiev, C.G. Park, H.S. Kim, Superior strength and multiple strengthening mechanisms in nanocrystalline TWIP steel. Sci. Rep. **8**, 11200 (2018). https://doi.org/10.1038/s41598-018-29632-y

46. H. Singh, D. Kumar, Validation of novel geometrically necessary dislocations calculation model using nanoindentation of the metal matrix nanocomposite. Metall. Mater. Trans. A **51**, 6700–6705 (2020). https://doi.org/10.1007/s11661-020-06016-4

47. Y.H. Jo, D.W. Kim, H.S. Kim, S. Lee, Effects of grain size on body-centered-cubic martensitic transformation in metastable Fe46Co30Cr10Mn5Si7V2 high-entropy alloy. Scr. Mater. **194**, 113620 (2021). https://doi.org/10.1016/j.scriptamat.2020.11.005

48. J. Liu, C. Chen, Q. Feng, X. Fang, H. Wang, F. Liu, J. Lu, D. Raabe, Dislocation activities at the martensite phase transformation interface in metastable austenitic stainless steel: An in-situ TEM study. Mater. Sci. Eng. A **703**, 236–243 (2017). https://doi.org/10.1016/j.msea.2017.06.107

49. D.A. Porter, K.E. Easterling, M.A. Sherif, *Phase Transformations in Metals and Alloys*, 3rd edn. (CRC Press, New York, 2009)

50. I. Tamura, Deformation-induced martensitic transformation and transformation-induced plasticity in steels. Met. Sci. J. **16**(5), 245–253 (1982). https://doi.org/10.1179/030634582790427316

51. J. Zhang, Y. Jiang, C. Hu, G. Ji, C. Song, O. Zhai. Effect of Cr on phase transformation behavior of austenite in Fe-20Mn-9Al-1.2C-xCr low-density steels during isothermal aging. Met. Mater. Int. **28**, 2583–2595 (2022). https://doi.org/10.1007/s12540-022-01167-y